JBIC Journal of Biological Inorganic Chemistry
https://doi.org/10.1007/s00775-018-1606-0

ORIGINAL PAPER

Aroylhydrazones constitute a promising class of 'metal-protein attenuating compounds' for the treatment of Alzheimer's disease: a proof-of-concept based on the study of the interactions between zinc(II) and pyridine-2-carboxaldehyde isonicotinoyl hydrazone

Daphne S. Cukierman[1] · Elio Accardo[1] · Rosana Garrido Gomes[1] · Anna De Falco[1] · Marco C. Miotto[2] · Maria Clara Ramalho Freitas[3] · Mauricio Lanznaster[4] · Claudio O. Fernández[2] · Nicolás A. Rey[1]

Received: 18 June 2018 / Accepted: 22 August 2018

Abstract

With the increasing life expectancy of the world's population, neurodegenerative diseases, such as Alzheimer's disease (AD), will become a much more relevant public health issue. This fact, coupled with the lack of efficacy of the available treatments, has been driving research directed to the development of new drugs for this pathology. Metal-protein attenuating compounds (MPACs) constitute a promising class of agents with potential application on the treatment of neurodegenerative diseases, such as AD. Currently, most MPACs are based on 8-hydroxyquinoline. Recently, our research group has described the hybrid aroylhydrazone containing the 8-hydroxyquinoline group INHHQ as a promising MPAC. By studying the known structure-related ligand HPCIH, which does not contain the phenol moiety, as a simplified chemical model for INHHQ, we aimed to clarify the real impact of the aroylhydrazone group for the MPAC activity of a compound with potential anti-Alzheimer's activity. The present work describes a detailed solution and solid-state study of the coordination of HPCIH with Zn^{2+} ions, as well as its in vitro binding-ability towards this metal in the presence of the Aβ(1–40) peptide. Similar to INHHQ, HPCIH is able to efficiently compete with Aβ(1–40) for Zn^{2+} ions, performing as expected for an MPAC. The similarity between the behaviors of both ligands is remarkable. Taken together, the data presented herein point to aroylhydrazones, such as the compounds HPCIH and the previously published INHHQ, as encouraging MPACs for the treatment of AD.

Keywords Aroylhydrazones · MPAC · Alzheimer's disease · Zinc(II) · Aβ peptide

Electronic supplementary material The online version of this article (https://doi.org/10.1007/s00775-018-1606-0) contains supplementary material, which is available to authorized users.

✉ Nicolás A. Rey
nicoarey@puc-rio.br

[1] Departamento de Química, Pontifícia Universidade Católica do Rio de Janeiro, Rio de Janeiro, RJ 22451-900, Brazil

[2] Max Planck Laboratory for Structural Biology, Chemistry and Molecular Biophysics of Rosario (MPLbioR, UNR-MPIbpC) and Instituto de Investigaciones para el Descubrimiento de Fármacos de Rosario (IIDEFAR, UNR-CONICET), Universidad Nacional de Rosario, S2002LRK Rosario, Santa Fe, Argentina

[3] Instituto de Química, Universidade Federal Rural do Rio de Janeiro, Seropédica, RJ 23890-000, Brazil

[4] Instituto de Química, Universidade Federal Fluminense, Niterói, RJ 24020-141, Brazil

Abbreviations

Aβ	β-Amyloid peptide
HPCIH	Pyridine-2-carboxaldehyde isonicotinoyl hydrazone
INHHQ	8-Hydroxyquinoline-2-carboxaldehyde isonicotinoyl hydrazone
MPACs	Metal-protein attenuating compounds

Introduction

Alzheimer's disease (AD) is a neurodegenerative disorder that currently represents the most common form of dementia in the elderly. The Aβ peptide is usually considered essential in the development of AD and is at the center of the amyloid cascade hypothesis, which postulates that this peptide itself and/or the cleavage products of its precursor protein, the

Published online: 25 August 2018

amyloid precursor protein (APP), are neurotoxic and can lead to the formation of senile plaques, causing neuron death [1]. The oligomeric hypothesis of AD is based on the amyloid cascade hypothesis, specifying that soluble Aβ oligomers are the most toxic aggregates [2, 3]. In its oligomeric form, Aβ immediately damages the neuronal synapses, leading to cell death [4].

Recently, quite a few studies have highlighted the role of endogenous metal ions in AD. It is suggested that such ions, particularly zinc(II) and copper(II), may contribute to Aβ aggregation, as well as, in the case of copper, to the increase of the aggregates' toxicity mediated by an amplified ROS production [5–11]. Both ions have been shown to raise the rate of aggregation of the synthetic Aβ peptide through the cross-binding to histidine residues [9, 12–14]. In addition, it is important to note that zinc(II) and copper(II) are poorly distributed in the brains of patients with AD [15–17].

Metal-protein attenuating compounds (MPACs) constitute an emerging class of therapeutic agents that may delay or even prevent the progression of AD. These are chelators that present a moderate affinity for certain metal ions and aim to avoid the accumulation and reduce the toxicity of Aβ oligomers in tissues [18]. MPACs should restore physiological metal homeostasis through the specific binding of zinc and copper, attenuating their abnormal interactions with the proteins in local excess, preventing their oligomerization and their ROS-mediated toxicity [19–21]. It is appropriate to state that the MPAC approach does not constitute an absolute unanimity among the researchers in the field of AD, mainly due to lack of clinical success of the 8-hydroxyquinoline derivatives clioquinol (PBT1) and PBT2. In a recent review, although with a major focus on copper, Simon C. Drew plays, in his own words, the devil's advocate, questioning the experimental evidence, the dogma, and the value of therapeutic chelation [22]. Nevertheless, the author admits that these previous failures "may reflect an inappropriate choice of chelator". Dr. Drew's point of view was contested in a General Commentary article by Rosanna Squitti et al., published some months later in the same journal [23], whose conclusions support the absence of a "valid reason for abandoning therapeutic chelation of copper ions in AD".

A few years ago, we have reported the crystal structure of 8-hydroxyquinoline-2-carboxaldehyde isonicotinoyl hydrazone (INHHQ, Scheme 1a) [24]. More recently, we demonstrated the MPAC capacity of this compound in competing for the interactions of Zn^{2+} and Cu^{2+} with the Aβ peptide [25], and of Cu^{+} and Cu^{2+} with α-Syn [26], in vitro.

In a similar context, Becker and Richardson described a series of chelators derived from the reaction between pyridine-2-carboxaldehyde and a number of hydrazides, the model compound being pyridine-2-carboxaldehyde isonicotinoyl hydrazone (HPCIH, Scheme 1b) [27]. The aroylhydrazone HPCIH has been extensively studied concerning its metal coordination abilities. In 2003, Armstrong et al. [28] described a sequence of complexes with divalent metal ions of the first transition series, from Mn^{2+} to Zn^{2+}, coordinated by HPCIH in a diversity of ways, including the complex $[Cu(PCIH)_2]$ and a polymeric structure of the type $[Zn(HPCIH)SO_4]_n$. Complexes with two and even three metal ions (di- and trinuclear, respectively) were also obtained, as in the case of a symmetric Mn^{2+} compound. More recently, mono- and dinuclear copper complexes of HPCIH have been reported, the former being obtained in the ML_2 stoichiometric ratio [29]. In 2015, Khandar et al. [30] synthesized a series of coordination polymers containing HPCIH and the Cd^{2+} ion. This metal is also interesting because although it does not belong to the first transition series, it is of the same family as zinc, and therefore, has similar chemical properties. In 2016, Li et al. [31] published the crystal structure of the complex $[ZnCl_2(HPCIH)]$.

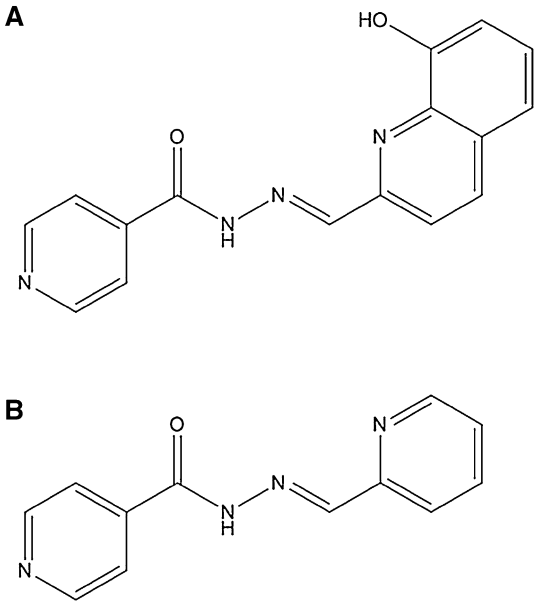

Scheme 1 Chemical structures of the aroylhydrazones. **a** INHHQ and **b** HPCIH

Since HPCIH is closely related to INHHQ in structural terms but lacks the fused phenolic ring present in the latter, it constitutes an excellent model of comparison to define the real contribution of the aroylhydrazone moiety for the MPAC activity of INHHQ. It is worth noting that, up to now, the 8-hydroxyquinoline scaffold present in ligands such as clioquinol, PBT2 and even the hybrid compound INHHQ remains the main chemical archetype in the development of new MPACs [32–35].

In this context, the present work describes a detailed solution and solid-state study of the coordination of HPCIH with Zn^{2+} ions, as well as its in vitro binding-ability towards this metal in the presence of the Aβ(1–40) peptide, aiming to

clarify some queries related to the true nature of the pharmacophore in INHHQ.

Materials and methods

Chemicals

All chemicals were obtained from commercial sources and employed without further purification, except for the pyridine-2-carboxaldehyde (an oily colorless liquid), which was distilled immediately prior to its use.

Synthesis of the ligand HPCIH: pyridine-2-carboxaldehyde isonicotinoyl hydrazone

The synthesis was performed according to Richardson et al. [36]. Yield: 58%. Elemental analysis—experimental % (calculated %): C 55.3 (55.0); H 5.4 (5.4); N, 21.8 (21.4). Formula: $C_{12}H_{10}N_4O{\cdot}2H_2O$ (262.26 g mol^{-1}).

Melting point: 172 ± 1 °C.

Synthesis of the zinc(II) complex (1)

The complex was prepared from the reaction between $HPCIH{\cdot}2H_2O$ (0.52453 g, 2.0 mmol) and anhydrous zinc(II) chloride (0.27263 g, 2.0 mmol) in methanol, at reflux for 3 h. The pale yellow precipitate was filtered off and washed with methanol. Yield: 0.5674 g (78%). Monocrystals suitable for X-ray crystallography were obtained from the mother liquor. Elemental analysis—experimental % (calculated %): C 39.4 (39.7); H 2.8 (2.8); N, 15.2 (15.4); Zn, 17.9 (18.0).

Formula: $[ZnCl_2(HPCIH)]$ ($C_{12}H_{10}N_4OCl_2Zn$, 362.43 g mol^{-1}).

TG studies show that there is no considerable mass loss below 300 °C, which indicates the absence of crystallization solvent in the structure.

Instrumentation, chemical characterization and in vitro studies

The carbon, hydrogen and nitrogen amounts in the samples were analyzed simultaneously on an EA112 thermo electron elemental analyzer (CHN), in duplicate. The determination of the melting point of the organic ligand was performed in a Fisatom apparatus, model 431, in triplicate. The percentage of zinc in the complex was determined by flame atomic absorption spectroscopy (FAAS) in a contrAA 700 Analytik Jena flame spectrophotometer, using Titrisol® standard. Thermogravimetric analyses were conducted in a Pyris 1 TGA Perkin-Elmer analyzer, under nitrogen atmosphere, in the 20–900 °C range with a heating rate of 10 °C min^{-1}.

IR spectra were recorded in the 4000–450 cm^{-1} (mid-infrared) and 700–100 cm^{-1} (far-infrared) ranges using a 100 FT-IR Perkin-Elmer absorption spectrophotometer. Samples were prepared in KBr pellets for the mid infrared, and in polyethylene or CsI pellets for the far-infrared measurements. Raman spectra were acquired in a Perkin-Elmer Station 400 spectrophotometer, in the region of 3500–200 cm^{-1}. Nuclear magnetic resonance spectra of hydrogen, carbon, and the contour maps $^1H \times {}^1H$ COSY, $^1H \times {}^{13}C$ HSQC and $^1H \times {}^{13}C$ HMBC were obtained on a 400 MHz Bruker-FT spectrophotometer at room temperature. A 5 mm BBO probe was used and samples were prepared in DMSO-d_6. Calibration was performed based on the residual solvent signal (quintet at 2.50 ppm for the H nucleus and septet at 39.52 for the C nucleus). All UV–Vis spectra were acquired on a Lambda 35 Perkin-Elmer molecular absorption equipment in the 200–800 nm range, at room temperature. A quartz cuvette with 1.0 cm optical path was employed. All solutions were prepared at low concentrations (5.0×10^{-5} mol l^{-1}) so that there was no precipitation throughout the experiments. For the stability in 10% DMSO/water assay, the initial scanning spectrum was obtained immediately after the addition of water and other spectra were acquired at regular intervals until the system was in equilibrium, i.e., until there was no further spectral change.

Single crystal X-ray diffraction data were collected on a Bruker D8 Venture diffractometer at room temperature, using a microfocus X-ray source, CuKα radiation ($\lambda = 1.54178$ Å) due to weak crystal diffraction. The crystal, selected with the help of an optical microscope using a polarized lens, was mounted in a polymeric loop (Mitegen micromount™) and fixed on a Kappa goniometer. Reflections were collected at room temperature, using a PHOTON 100 detector with a CMOS sensor. Data collection and cell refinement were performed with Bruker Instrument Service APEX2 v4.2.2 [37]. Data integration was carried out using SAINT [38] with a resolution of 0.83 Å. The structure solution, using direct methods, was performed with SHELXS-2013. The full-matrix least-squares refinements, based on F^2, were done using the SHELXL-2013 program package [39], in Wingx software interface [40]. Anisotropic parameters were refined to all non-hydrogen atoms, and a constraint was used for the disordered chloride counter ions. Positions of the hydrogen atoms were constrained to neutral diffraction distance values [41]. Crystallographic tables were organized using the OLEX2 software [42].

Polycrystalline samples were studied according to the Bragg–Brentano geometry on a Bruker D8 Discover diffractometer at room temperature. The 2θ sweep was done from 5° to 90°, with a counting time per step of 1 s and a step size of 0.02°.

Electrospray ionization mass spectrometry (ESI-MS) analyses were collected on a Perkin-Elmer SQ-300 mass

spectrometer. Stock solutions of the samples were prepared by dissolving 1.0 mg of HPCIH and its zinc(II) complex in 1.0 ml of DMSO. Aliquots of 50 µl of these solutions were diluted in 950 µl of methanol and analyzed by direct infusion. The standard configuration parameters for the two modes, positive and negative, were used except for the capillary output voltage (CAPEX), set at 50 V.

The isothermal titration calorimetry studies were carried out in a MicroCal ITC microcalorimeter, at room temperature. Briefly, 2.0 mL of a 100 µmol l^{-1} ligand solution was prepared in 5% DMSO/95% 20 mM HEPES buffer, pH 6.8, which was introduced into the reaction cell. A 1.0 mmol l^{-1} solution of zinc(II) sulfate in 5% DMSO/95% H_2O was introduced into the injection syringe with a total volume of 450 µl. 2.0 ml of the reference solution containing 5% DMSO/95% H_2O was also prepared. Care was taken to eliminate all bubbles present in the solutions.

For the interactions with the Zn(II)-Aβ system, NMR spectra were acquired on a Bruker Avance III 600 MHz spectrometer using a cryogenically cooled triple resonance $^{1}H(^{13}C/^{15}N)$ TCI probe. 2D $^{1}H–^{15}N$ HSQC experiments were performed on 50 µM ^{15}N-labeled Aβ(1–40) peptide samples dissolved in buffer A (20 mM MES buffer supplemented with 100 mM NaCl, pH 6.5) at 15 °C using standard pulse sequences from the Topspin suite (Bruker) library. Aggregation did not occur under these low temperature conditions and the absence of stirring. For the mapping experiments, $^{1}H–^{15}N$ amide cross-peaks affected during HPCIH titration in the presence of Zn^{2+} were identified by comparing their intensities (I) with those of the same cross-peaks in the data set of samples containing one equivalent of the divalent metal ion (I_0). The I/I_0 ratios of non-overlapping cross-peaks were plotted as a function of the peptide sequence to obtain the intensity profiles. Acquisition and processing of spectra were made using TOPSPIN 3.2 (Bruker Biospin). 2D spectra analysis and visualization were performed with CCPN.

The distribution coefficient (P) in the 1-octanol/water system was calculated using the shake flask method. A pH 7.40 buffer was employed as the aqueous phase. Both phases, organic and aqueous, were pre-saturated with the hydrazone at low concentrations (5×10^{-5} mol l^{-1}). Then, the UV–Vis spectrum was recorded for each phase before mixing them together. The vial containing the mixture was shaken vigorously at 37.0 °C, protected from light, for 3 h (ThermoShaker, KASVI). At the end of the incubation, the mixture was centrifuged for 10 min at 3000 rpm, and the layers were separated with a Pasteur pipette. Concentrations in both phases were measured in the wavelength of higher absorption for each hydrazone, through individual calibration curves. Each compound was analyzed in triplicate and P was determined as the average concentration ratio C_o/C_w, where C_o is the final concentration in the organic phase and C_w is the final concentration in the aqueous phase. Log P was calculated and compared with the values obtained from in silico analyses, performed in the program Osiris Property Explorer: DataWarrior™, software freely available for download at http://www.organic-chemistry.org/prog/peo/, accessed on 15/11/2017.

Results and discussion

Solid-state characterization of HPCIH and Zn^{2+}–HPCIH complexes

Thermogravimetric analysis (TG)

The thermogravimetric analysis is important to determine the amount of solvent molecules in the structure of a compound so that the exact molar mass could be used in further studies. Thermal decomposition of HPCIH occurs in two steps (Figure S1—Supplementary Information). The first stage, when occurring around 100 °C, is usually associated with the loss of hydration water. The mass loss percentage of the first step obtained for HPCIH is consistent with the presence of two water molecules, which confirms the results obtained by elemental analysis and the composition described in the original patent application about this ligand [36]. The second mass loss step corresponds to the total degradation of HPCIH. After 350 °C, there is no more residue left.

Vibrational spectroscopy

The main infrared and Raman bands of HPCIH·$2H_2O$ and complex (**1**), along with the probable assignments, are shown in Table 1. All the vibrational spectra can be found in the Supplementary Information, as Figures S2 and S3.

A very evident spectral change in the complex with respect to the ligand is related to the displacement of the band corresponding to the C=O stretching, which goes from 1663 cm^{-1} in free HPCIH to 1649 cm^{-1} in (**1**) (Raman: 1656 cm^{-1} to 1644 cm^{-1}), suggesting the involvement of this group in coordination. On the other hand, the ν(C=N) mode of azomethine is usually not susceptible to changes upon complexation and remains unshifted in the spectrum of the complex. However, the participation of this group in the coordination of zinc can be inferred by the change of its ν(CH) absorption, which is downshifted from 2853 to 2826 cm^{-1} upon complexation. An additional spectral feature indicating the involvement of the aroylhydrazone moiety in coordination is an upshift of the ν(N–N) associated band, which was assigned at 1146 cm^{-1} in free HPCIH (Raman: 1142 cm^{-1}) and is observed at 1165 cm^{-1} (Raman: 1162 cm^{-1}) in the spectrum of (**1**). As expected, the mid-infrared bands related to the pyridine ring demonstrated not

Table 1 Selected IR and Raman frequencies of HPCIH·$2H_2O$ and (**1**), along with their assignments

Assignment	HPCIH		(1)	
	IR (cm^{-1})	Raman (cm^{-1})	IR (cm^{-1})	Raman (cm^{-1})
ν(NH)	3450	–	3455	–
$\nu(OH)_{water}$	3270	–	–	–
$\nu(CH)_{aromatic}$	3072/3030	3070	3070/3040	3072/3035
$\nu(CH)_{azomethine}$	2853	–	2826	–
ν(C=O)	1663	1656	1649	1644
$\nu(C=N)_{azomethine}$	1621	1615	1626	1624
$\nu(C=N)_{pyridine}$	1606	1605	1598	1600
$\nu(C=C)_{aromatic}$	1571	1565	1570	1568
	1472	1472	1470	1472
ν(N–N)	1146	1142	1165	1162
ν(Zn–O)	–	–	415	–
ν(Zn–Cl)	–	–	330/300	328/304
$\nu(Zn–N)_{pyridine}$	–	–	204	200

to be very sensitive to complexation. Moreover, the presence of two different pyridine rings in HPCIH makes the interpretation of any spectral change related to these heteroaromatic systems even more difficult.

The far-infrared spectrum of (**1**) showed the appearance of bands related to some vibrational modes involving the coordination sphere of zinc. For example, the ν(Zn–O) absorption can usually be found around 360 cm^{-1} [43], and was assigned at 415 cm^{-1} in the spectrum of the complex. Two other new bands at 330 and 300 cm^{-1} were attributed, respectively, to the asymmetric and symmetric stretching modes of Zn–Cl bonds [44]. At last, absorptions regarding the stretching of zinc binding to pyridine nitrogen, ν(Zn–N), are observed by 200 cm^{-1} [45]. In (**1**), the band at 204 cm^{-1} was assigned to this mode.

X-ray diffraction

Although the solid collected in the synthesis corresponds to the discrete compound [$ZnCl_2$(HPCIH)] (**1**), the monocrystals obtained from the mother liquor of this complex are constituted of a novel one-dimensional polymer network [complex (**2**), Fig. 1], containing [$Zn_2Cl_2(HPCIH)_2$]Cl_2 (composed by two isostructural, although non-equivalent in the solid-state, forms of the coordination compound) as the asymmetric unit. The solid belongs to the monoclinic

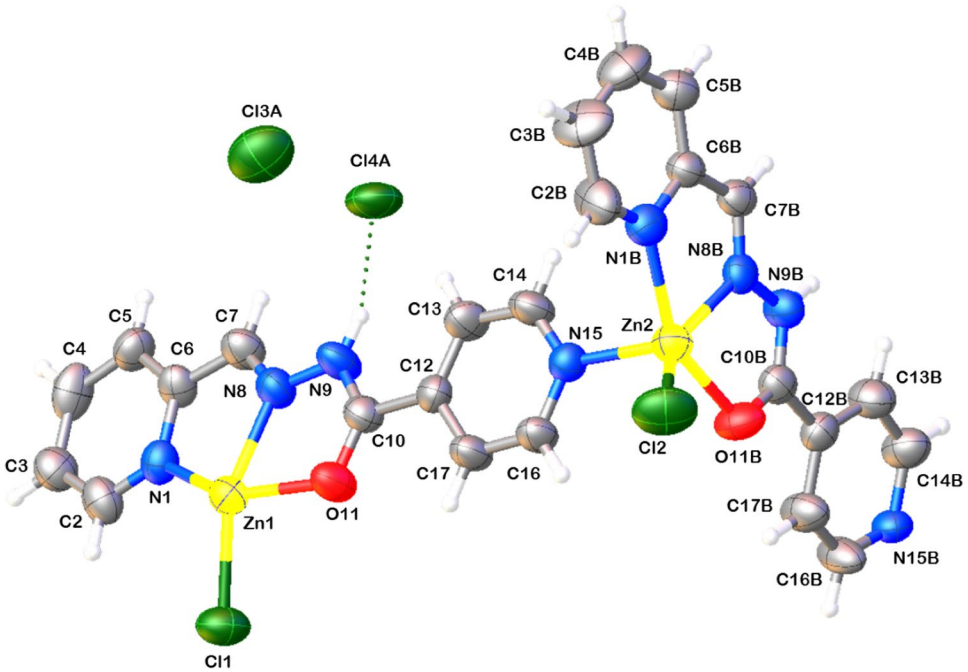

Fig. 1 Asymmetric unit in complex (**2**). Disordered chloride ions were omitted for the sake of clarity

system, $P2_1/c$ space group. Crystal, data collection and refinement parameters are summarized in Table 2. Selected bond distances and angles can be found in Table 3.

In both forms, HPCIH coordinates in a tridentate manner through the N1/N1B pyridine nitrogen atom and the N8/N8B and O11/O11B atoms, the latter two belonging to the aroylhydrazone system. A chloro ligand (Cl1/Cl2) completes the equatorial plane of the zinc coordination sphere. The N15B/N15 nitrogen atom of the respective non-equivalent complex unit occupies the axial position, thus closing the metals' almost perfect square-pyramidal coordination pattern (Zn1 and Zn2 are both pentacoordinated, with τ values around 0.05). In this sense, we can consider that the (*E*) isomer of HPCIH coordinates in the N_3O-chelating–bridging mode. These results suggest that after some time in solution, one of the chloro ligands of complex (**1**) is replaced by a solvent molecule which, in turn, throughout the slow evaporation process that led to the formation of the crystal, leaves the metal center so that the monomer units can interact with each other through the previously uncoordinated N15B/N15 nitrogen atom, giving rise to the coordination polymer (**2**). In the crystallographic model proposed, HPCIH is in its protonated form at N9/N9B, corresponding to the keto-amine tautomer. The complex neutrality is achieved by the presence of two chloride counter ions, disordered between two statical positions in a proportion of about 50%.

Details of the 1D zig-zag polymeric structure are displayed in Fig. 2.

On the other hand, the structure of compound $[ZnCl_2(HPCIH)]$ (**1**), synthesized in a dichloromethane–methanol solvent mixture, was published on January 2016 by researchers in China and the US [31]. In this structure, zinc exhibits a distorted square-pyramidal geometry, with $\tau = 0.19$. The axial position is occupied by a chloro ligand, whereas in our coordination polymer, as stated above, the N15B/N15 nitrogen of another ligand unit occupies such a position. The equatorial bonding distances of the coordinating sphere of the Zn1/Zn2 centers at complex (**2**) were compared to those concerning the published compound, $[ZnCl_2(HPCIH)]$. The bonds to N1/N1B, N8/N8B and O11/O11B are smaller in complex (**2**), whereas zinc-chloro distances are the same in both structures.

Finally, the simulated diffractogram from the structural data published by Li et al. was compared with that of complex (**1**). The small discrepancies between the diffractograms can be attributed to subtle differences in network packaging, generating a polymorph. This is further evidence of the chemical identity of (**1**), which we propose to be a microcrystalline form of the complex published in 2016 (Fig. 3).

Table 2 Crystallographic data for complex (**2**)

Empirical formula	$C_{12}H_{10}N_4OCl_2Zn$
Formula weight	362.54
Temperature/K	293.15
Crystal system	Monoclinic
Space group	$P2_1/c$
a/Å	10.4609(3)
b/Å	19.2990(7)
c/Å	15.4176(4)
α/°	90
β/°	104.675(2)
γ/°	90
Volume/Å^3	3011.04(16)
Z	8
ρ_{calc} g/cm^3	1.521
μ/mm^{-1}	4.711
F(000)	1388.0
Crystal size/mm^3	0.109 × 0.074 × 0.048
Radiation	CuKα ($\lambda = 1.54178$)
Reflections collected	41021
Independent reflections	5722 [$R_{int} = 0.1705$, $R_{sigma} = 0.1064$]
Data/restraints/parameters	5722/0/381
Goodness-of-fit on F^2	0.999
Final *R* indexes [$I \geq 2\sigma(I)$]	$R_1 = 0.0697$, $wR_2 = 0.1653$
Final *R* indexes [all data]	$R_1 = 0.1694$, $wR_2 = 0.2157$
Largest diff. peak/hole/e Å^{-3}	0.57/− 0.43

Table 3 Selected bond distances and angles for complex (**2**)

Bond distance/Å			
Zn1–N1	2.206(7)	Zn2–N1B	2.175(7)
Zn1–N8	2.089(7)	Zn2–N8B	2.050(7)
Zn1–O11	2.114(6)	Zn2–O11B	2.137(6)
Zn1–N15B^1	2.068(7)	Zn2–N15	2.062(7)
Zn1–Cl1	2.228(3)	Zn2–Cl2	2.215(3)
C7–N8	1.263(10)	C7B–N8B	1.295(9)
C10–O11	1.279(9)	C10B–O11B	1.267(9)
Bond angles/°			
N1–Zn1–N8	75.5(3)	N1B–Zn2–N8B	75.7(3)
N1–Zn1–O11	147.4(3)	N1B–Zn2–O11B	149.4(3)
N1–Zn1–N15B^1	95.4(3)	N1B–Zn2–N15	96.9(3)
N1–Zn1–Cl1	99.7(2)	N1B–Zn2–Cl2	101.8(2)
N8–Zn1–O11	74.1(3)	N8B–Zn2–O11B	73.9(2)
N8–Zn1–N15B^1	102.1(3)	N8B–Zn2–N15	107.4(3)
N8–Zn1–Cl1	150.1(2)	N8B–Zn2–Cl2	146.3(2)
O11–Zn1–N15B^1	102.1(3)	O11B–Zn2–N15	95.4(2)
O11–Zn1–Cl1	100.83(18)	O11B–Zn2–Cl2	101.47(19)
N15B^1–Zn1–Cl1	107.7(2)	N15–Zn2–Cl2	106.3(2)

Symmetry code: $^1 1 - x, -½ + y, ½ - z$

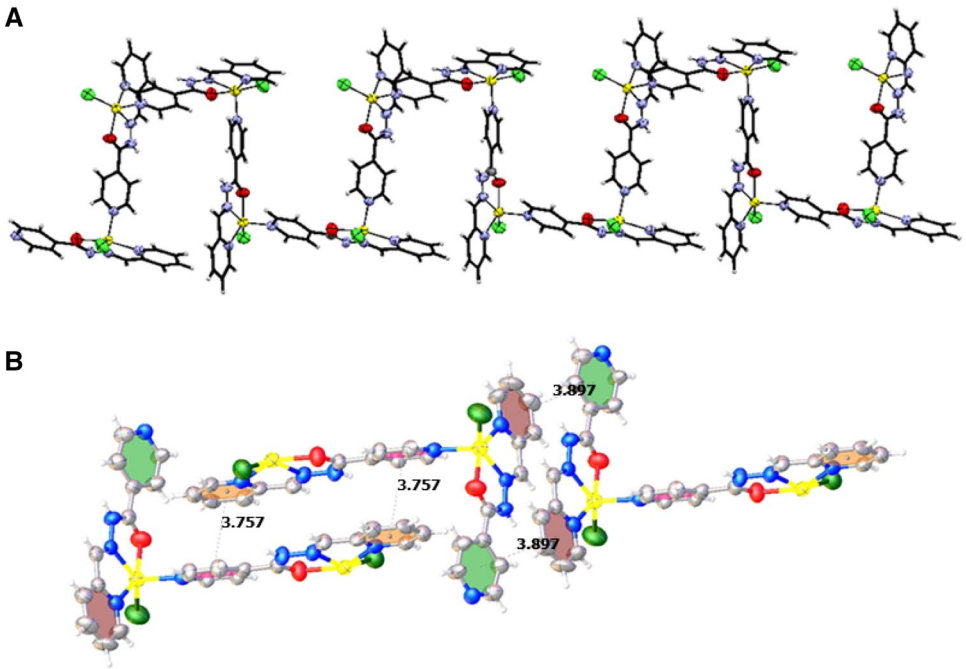

Fig. 2 **a** 1D zig-zag polymeric structure of complex (**2**). Yellow ellipsoids correspond to zinc(II) ions. **b** π–π packing interactions present in the solid state

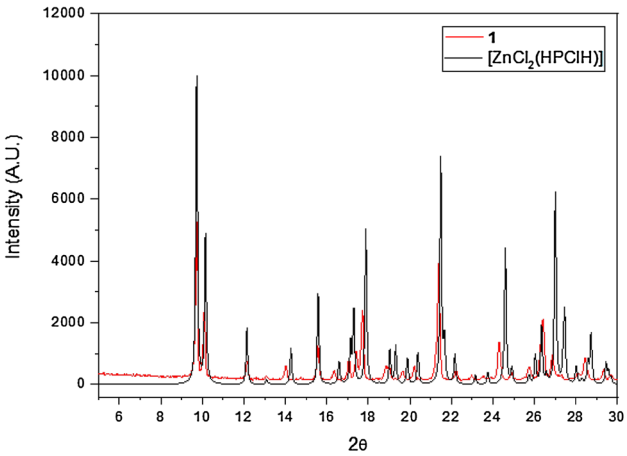

Fig. 3 Comparison, at the small angle limit, between the diffractograms of 1 and that simulated for [$ZnCl_2$(HPCIH)] from the original data published by Li et al.

Solution studies on HPCIH and Zn^{2+}–HPCIH complexes

Nuclear magnetic resonance (NMR)

The ^{1}H spectrum of HPCIH clearly shows three sets of signals (Figure S4), which indicates the presence of three species in solution (Scheme 2). For each of the three systems, it is possible to observe eight different resonances corresponding to the ten hydrogens of the molecule, since there are two cases of magnetic equivalence. The relative integration of the signals allowed concluding that there are 85% of the (*E*)-keto-amine and 14% of the (*E*)-enamine tautomers and 1% of the (*Z*)-keto-amine isomer. The most deshielded signals in the ^{1}H spectrum correspond to the N9–H (keto-amines) or to the O11–H (enamine) nucleus. For the (*E*)-keto-amine isomer, this signal is observed at 12.26 ppm due to the interaction of N9–H with the solvent, with a slight overlap of the signal of O11–H of its (*E*)-enamine tautomer. In contrast, the (*Z*)-keto-amine isomer shows the most deshielded signal, at 15.75 ppm, due to an N9–H···N1 intramolecular hydrogen bond (Scheme 2). Two-dimensional ^{1}H × ^{1}H COSY experiment (Figure S5) was used to univocally assign the ^{1}H signals. The ^{1}H × ^{13}C HMBC (Figure S6) contour plot allows differentiating the H16/H14 pair from the H13/H17 one, since the C10 signal has correlations of different intensities with each of them.

In the ^{13}C spectrum (Figure S7), just ten signals, regarding the twelve carbons of the molecule, are observed. Since the isotopic abundance of ^{13}C is very low, only the predominant keto-amine tautomer of the (*E*)-isomer could be detected. 2D heteronuclear (^{1}H × ^{13}C) experiments HSQC (Figure S8) and HMBC allowed for a complete assignment of the ^{13}C resonances.

Table 4 summarizes the attributions made for the ^{1}H and ^{13}C signals of the foremost (*E*)-keto-amine species.

In the same way as for the ligand, the ^{1}H spectrum of (**1**) led us to infer the presence of three species in DMSO-d_6 solution, since dissolution promotes the partial deprotonation of the coordinated ligand. However, the integration of the third set of signals was negligible. The relative integration of the hydrogen signals allowed us to conclude that the majority of the complex molecules in solution are in the

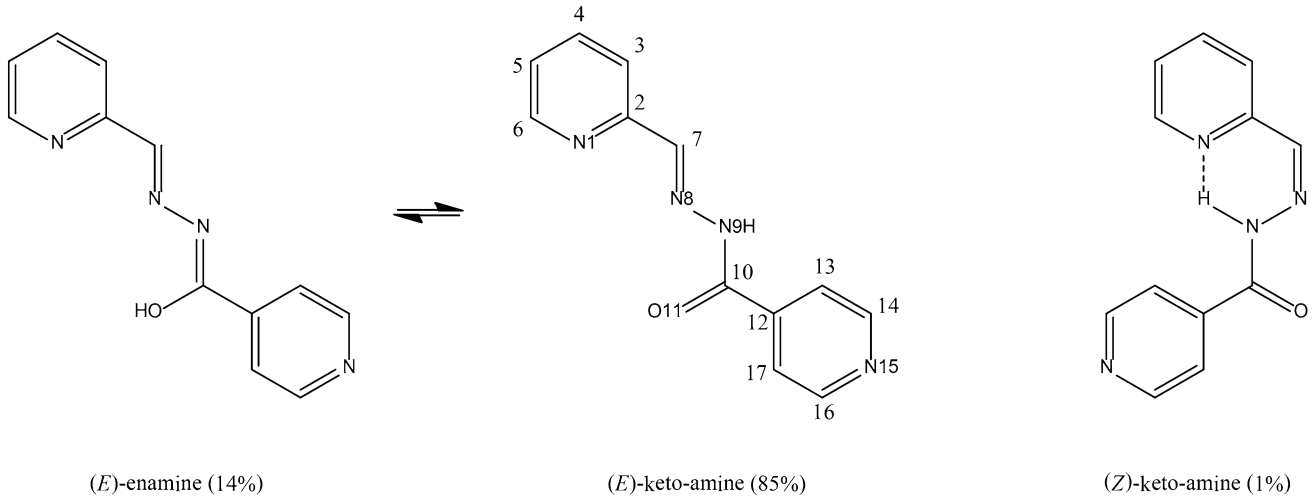

Scheme 2 Chemical forms of HPCIH present in a DMSO-d_6 solution at room temperature

Table 4 ^{1}H (400 MHz) and ^{13}C NMR data for HPCIH and (**1**) in DMSO-d_6 at room temperature

C/H	HPCIH			(1)	
	C (ppm)	H (ppm)	^{1}H × ^{13}C HMBC	C (ppm)	H (ppm)
2	153.90	–	H7 ($^{2}J_{CH}$) H4 ($^{3}J_{CH}$) H6 ($^{3}J_{CH}$)	152.23	–
3	121.10	8.00 (dd, 1H, ^{3}J = 7.9 Hz, ^{4}J = 1.1 Hz)	H7 ($^{3}J_{CH}$) H5 ($^{3}J_{CH}$)	120.83	8.00 (d, 1H, ^{3}J = 7.8 Hz)
4	137.96	7.90 (td, 1H, ^{3}J = 7.9 Hz, ^{3}J = 7.4 Hz, ^{4}J = 1.5 Hz)	H6 ($^{3}J_{CH}$)	137.50	7.94 (t, 1H, ^{3}J = 7.8 Hz)
5	125.66	7.45 (ddd, 1H, ^{3}J = 7.4 Hz, ^{3}J = 4.9 Hz, ^{4}J = 1.1 Hz)	H3 ($^{3}J_{CH}$) H6 ($^{2}J_{CH}$)	125.00	7.48 (dd, 1H, ^{3}J = 7.8 Hz, ^{3}J = 4.6 Hz)
6	150.58	8.63 (dd, 1H, ^{3}J = 4.9 Hz, ^{4}J = 1.5 Hz)	H4 ($^{3}J_{CH}$) H5 ($^{2}J_{CH}$)	149.47	8.64 (d, 1H, ^{3}J = 4.6 Hz)
7	150.20	8.49 (s, 1H)	H3 ($^{3}J_{CH}$)	149.07	8.52 (s, 1H)
N9H	–	12.26 (s, 1H)	–	–	–
10	162.90	–	H14/H16 ($^{4}J_{CH}$) H13/H17 ($^{3}J_{CH}$)	*	–
12	141.20	–	H14/H16 ($^{3}J_{CH}$)	140.84	–
13/17	122.54	7.84 (d, 2H, ^{3}J = 4.5 Hz, ^{4}J = 1.6 Hz)	H17/H13 ($^{3}J_{CH}$) H14/H16 ($^{2}J_{CH}$)	121.87	7.90 (d, 2H, ^{3}J = 5.7 Hz)
14/16	151.36	8.80 (dd, 2H, ^{3}J = 4.5 Hz, ^{4}J = 1.6 Hz)	H16/H14 ($^{3}J_{CH}$) H13/H17 ($^{2}J_{CH}$)	150.03	8.82 (d, 2H, ^{3}J = 5.7 Hz)

S, singlet; d, doublet; dd, doublet of doublets; td, triplet of doublets; ddd, doublet of doublet of doublets

*This signal was not observed in the spectrum of the complex

form of the deprotonated (*E*) isomer (enamine, 85%), being the remainder the protonated (*E*) isomer (keto-amine), as observed through the most deshielded signal at 12.28 ppm, corresponding to H9, which only appears in the protonated form. The one-dimensional ^{1}H and ^{13}C spectra and the two-dimensional COSY and HSQC spectra related to the complex are shown in Figures S9 to S12.

Scheme 3 shows the two species observed in solution.

Thus, the main system (most abundant) is composed of seven signals, which correspond to the nine hydrogen atoms of the molecule, since there are two cases of magnetic equivalence. Alternatively, the secondary system has eight signals, relative to ten hydrogens (there is an extra hydrogen due to the protonation of $PCIH^{-}$).

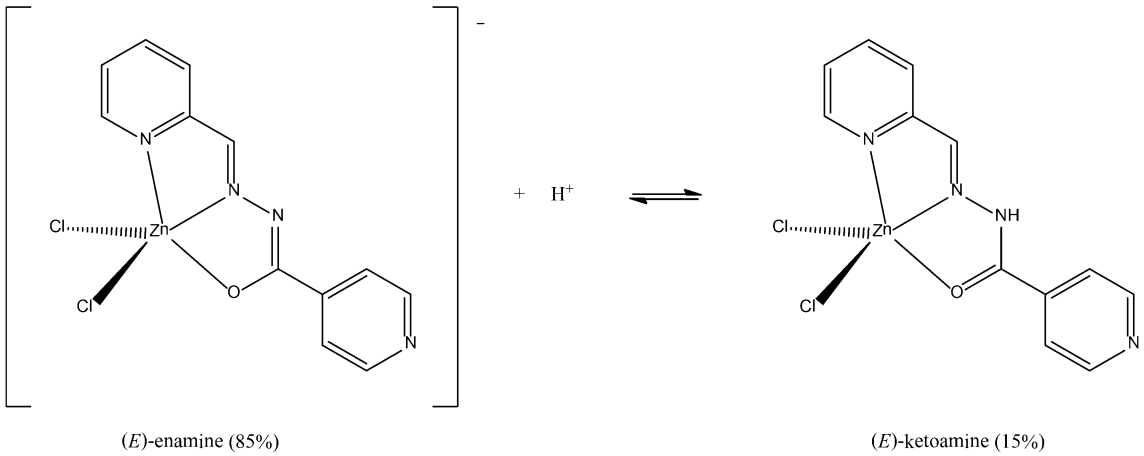

(*E*)-enamine (85%) (*E*)-ketoamine (15%)

Scheme 3 Species of the complex present in DMSO-d_6 solution at room temperature

Table 4 also contains the ^{1}H and ^{13}C NMR data related to the major species present in a DMSO-d_6 solution of (**1**), allowing for a straightforward comparison to the chemical shifts observed for free HPCIH. It can be seen that the hydrogen signals are slightly deshielded with the coordination of the metal and the carbon signals are, inversely, slightly shielded. The couplings occurring in the ligand remain in (**1**).

UV–Vis molecular absorption spectroscopy

Just an asymmetric band, centered at 301 nm, is observed in a DMSO solution of HPCIH, which was ascribed to a $\pi \rightarrow \pi^*$ transition (20,570 l mol^{-1} cm^{-1}, apparent molar absorptivity). The UV–Vis spectrum was also recorded in methanol, since the absence of the absorption of DMSO (UV cutoff around 270 nm) allows performing the curve-fitting of the band at 302 nm, which actually corresponds to two absorption components calculated at 271 and 305 nm, as well as observing a higher energy band, centered at 211 nm (Fig. 4a). This absorption might be related to the pyridine ring, present in both precursors: pyridine-2-carboxaldehyde and isonicotinic acid hydrazide (Fig. 4b, blue and green lines). The apparent molar absorptivity related to the 302 nm band in methanol was determined to be 23,220 l mol^{-1} cm^{-1}, close to that observed for the compound in DMSO. This $\pi \rightarrow \pi^*$ absorption is certainly related to the hydrazone group, since it is completely absent in the precursor compounds (Fig. 4b). In view of its lower transition energy, it may involve electronic delocalization to the pyridine rings.

It is well-known that hydrazones are potentially susceptible to hydrolysis when in a medium containing water. UV–Vis spectroscopy was therefore used to study the hydrolytic stability of the ligand at 25 °C in a 10% DMSO/water solution over 12 h. The band followed was that at 301 nm, since, as stated above, it is directly related to the hydrazone group. At the end of this period, there was only a 15.8% decrease in the intensity of the HPCIH absorption. On this basis, it was concluded that HPCIH is quite resistant to hydrolysis under the conditions of the present study (Figure S13).

The study of (**1**) was extended using molecular absorption spectroscopy under UV–visible light, in methanol (Fig. 5). At first sight, it is evident that complexation induces a hypochromic effect in the bands of HPCIH, all along the studied spectral window. Upon Fit-Peak performing, three absorptions can be clearly recognized: two shifted bands related to HPCIH, centered at 295 and 310 nm, and another one at 370 nm, a region where the free ligand does not absorb, which was assigned to a MLCT transition. The dependence of this last absorption on solvent polarity (data not shown) and the fact that the ion Zn^{2+} has fully occupied metal-centered orbitals and HPCIH possesses empty π antibonding orbitals support our proposition.

Electrospray ionization mass spectrometry (ESI-MS)

The mass spectrum of (**1**) in the positive mode (Fig. 6a) presents five relevant peaks at (m/z^+) 324.9, 332.9, 403.0 and 515.1 assigned to zinc-containing species, in addition to the most intense peak found at (m/z^+) 227.0 attributed to the free ligand HPCIH+H^+ ($C_{12}H_{11}N_4O^+$). The peaks at 403.0 and 515.1 were unequivocally assigned to the species $[ZnCl(DMSO)(HPCIH)]^+$ and $[Zn(HPCIH)(PCIH)]^+$, respectively, based on the isotopic distribution analysis shown in Fig. 6b, c. Thus, besides the presence of free ligand, the ML and ML_2 stoichiometries were clearly identified. The species $\{[ZnCl(DMSO)(PCIH)]+H^+\}^+$ results from the exchange of the coordinated chloro ligand by a DMSO molecule. The detection of this species indicates a

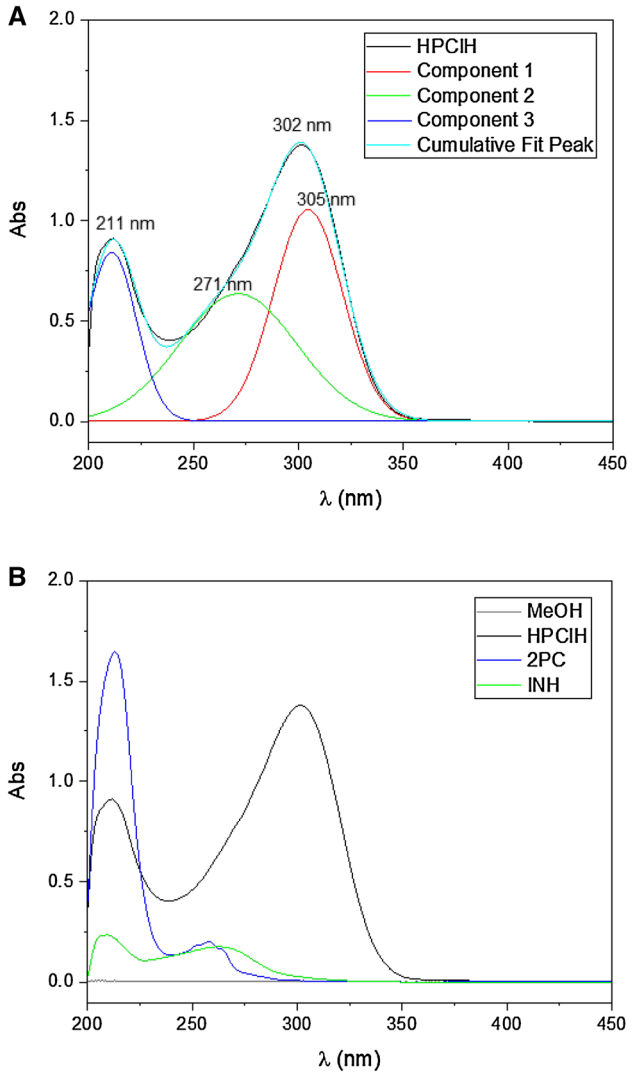

Fig. 4 Electronic spectrum of HPClH (5×10^{-5} mol l^{-1}) in methanol solution at room temperature. **a** Fit peak performed in Origin™ 2018. **b** Comparison to the spectra of precursors (5×10^{-5} mol l^{-1}) and pure solvent

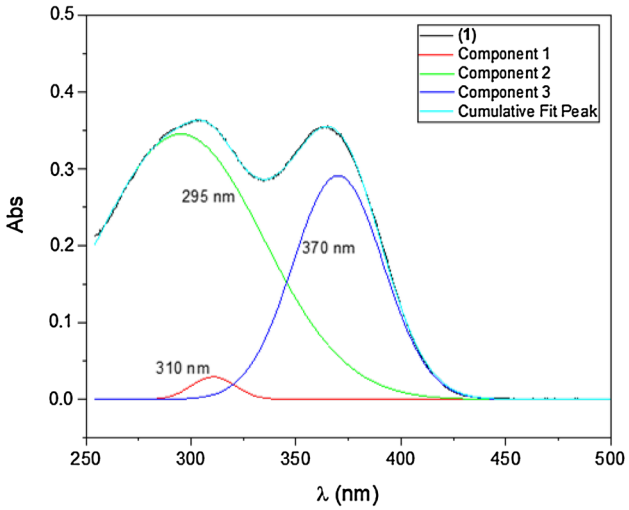

Fig. 5 Electronic spectrum of **1** (5×10^{-5} mol l^{-1}) in methanol solution at room temperature. Fit Peak performed in Origin™ 2018

strong affinity for DMSO by the complex, even in a methanol rich medium [46].

The ESI-MS spectrum recorded in the negative mode (Fig. 7) revealed the presence of $[ZnCl_2(PCIH)]^-$ ($C_{12}H_9N_4OCl_2Zn^-$), at (m/z^-) 359.0, generated from (**1**) by the deprotonation of the coordinated HPCIH ligand. Its identity was confirmed by the calculated isotopic distribution displayed in Fig. 7c, which fits perfectly with the experimental pattern. This confirms the assignment of the NMR spectrum as a result of two main species in solution, $[ZnCl_2(PCIH)]^-$ and $[ZnCl_2(HPCIH)]$. The latter could not be detected in the MS spectrum due to its neutral charge. The presence of the free ligand and two additional zinc(II) species in solution was also observed.

The peaks at (m/z^-) 168.9 and 493.0 were assigned to the species $[ZnCl_3]^-$ and $[Zn_2Cl_4(PCIH)]^-$ ($C_{12}H_9N_4OCl_4Zn_2^-$), respectively, and confirmed by their isotopic distribution analyses (Fig. 7b, d). The last species is most probably generated in the ESI interface, as it is not expected to be present in solution. The uncoordinated ligand was also found in its fully deprotonated anionic form $[PCIH]^-$, and associated with a chloride anion $[HPCIH+Cl]^-$ at (m/z^-) 225.0 and 261.1, respectively.

Isothermal titration calorimetry (ITC)

The resulting titration curve of HPCIH with Zn^{2+} ions at 25 °C is shown in Fig. 8 and the obtained stoichiometry, binding constant, enthalpy and entropy values for the reaction are presented in Table 5.

A *M*/*L* ratio of 0.462, corresponding to a ML_2 stoichiometry, was observed. It is worth noting that this stoichiometry was also identified in the ESI-MS experiments.

Moreover, the value of the overall formation constant (log β) of the complex $[Zn(PCIH)_2]$ was calculated using the obtained value of ΔG (− 29.43 kJ mol^{-1}) and the acid constant (pK_a) of the ligand retrieved from the literature [47]. A log $\beta = 14.33$ at 25 °C was obtained. Armstrong et al. [28] reported the log β value for the HPCIH complex with Zn^{2+} of ML_2 stoichiometry, obtained by potentiometry at 25 °C, as 13.85, a value that is in line with the one obtained in the present work.

Anti-Alzheimer's potential of the hydrazone HPCIH

In vitro interactions of HPCIH with Zn(II)-Aβ (MPAC-like activity)

As previously reported [25], the spectral changes observed upon addition of Zn^{2+} to the Aβ(1–40) samples were

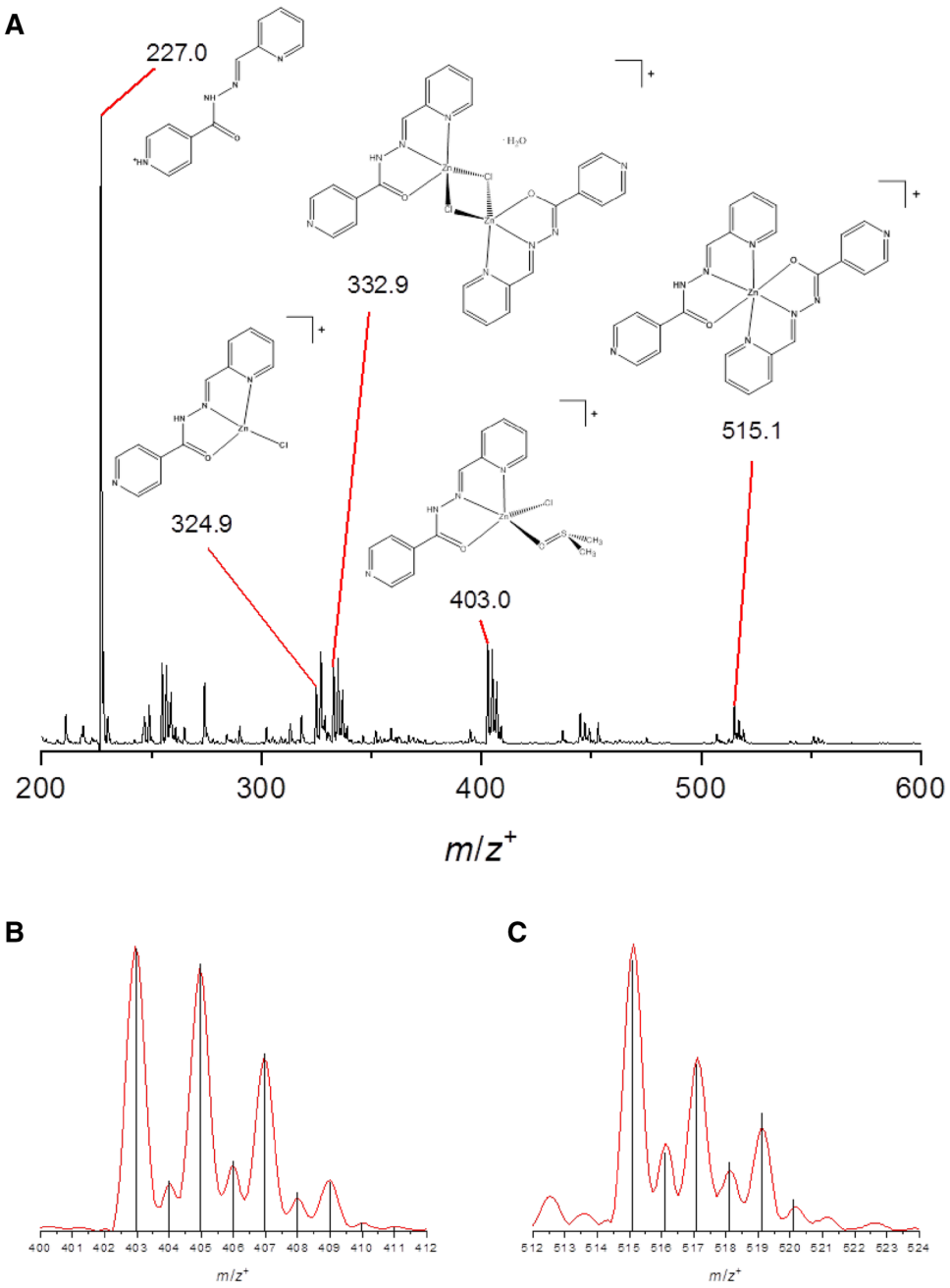

Fig. 6 **a** ESI-MS spectrum (positive mode) of (**1**) in a DMSO/methanol (5:95) mixture. **b** Isotope distribution of $[ZnCl(DMSO)(HPCIH)]^+$ ($C_{14}H_{16}N_4O_2ClSZn^+$). **c** Isotope distribution of $[Zn(HPCIH)(PCIH)]^+$ ($C_{24}H_{19}N_8O_2Zn^+$). Experimental and calculated data are shown, respectively, as red and vertical black lines, respectively

centered on residues Asp1, His6, His13, and His14, clearly indicating their involvement as metal coordinating sites for this physiological ion (Fig. 9a). The peptide's affected resonances were severely broadened by the addition of sub-stoichiometric concentrations of Zn^{2+} (Fig. 9c), whereas further addition up to 1 equivalent of the metal ion caused the Glu3, Phe4, Arg5, Asp7, Glu11, Val12, His13, Gln15 and Lys16 signals to be broadened beyond detection, indicative of a system undergoing intermediate exchange on the NMR chemical shift timescale. Interestingly, as shown in Fig. 9b, c, increasing amounts of HPCIH efficiently compete for the binding to Zn^{2+} ions, completely removing the metal-induced perturbations in the Aβ(1–40) backbone amides upon addition of 10 equivalents of the compound. This behavior resembles that of the INHHQ compound previously described by our research group, which was also able to recover almost completely the free peptide signals after the addition of five equivalents of ligand [25]. Moreover, we observed that the ^1H NMR spectrum of the peptide remained unchanged in the presence of HPCIH (data not shown), indicating that the compound does not interact directly with Aβ(1–40).

Calculating the exact value for the dissociation constant of the zinc(II) bound peptide can be difficult, since it is

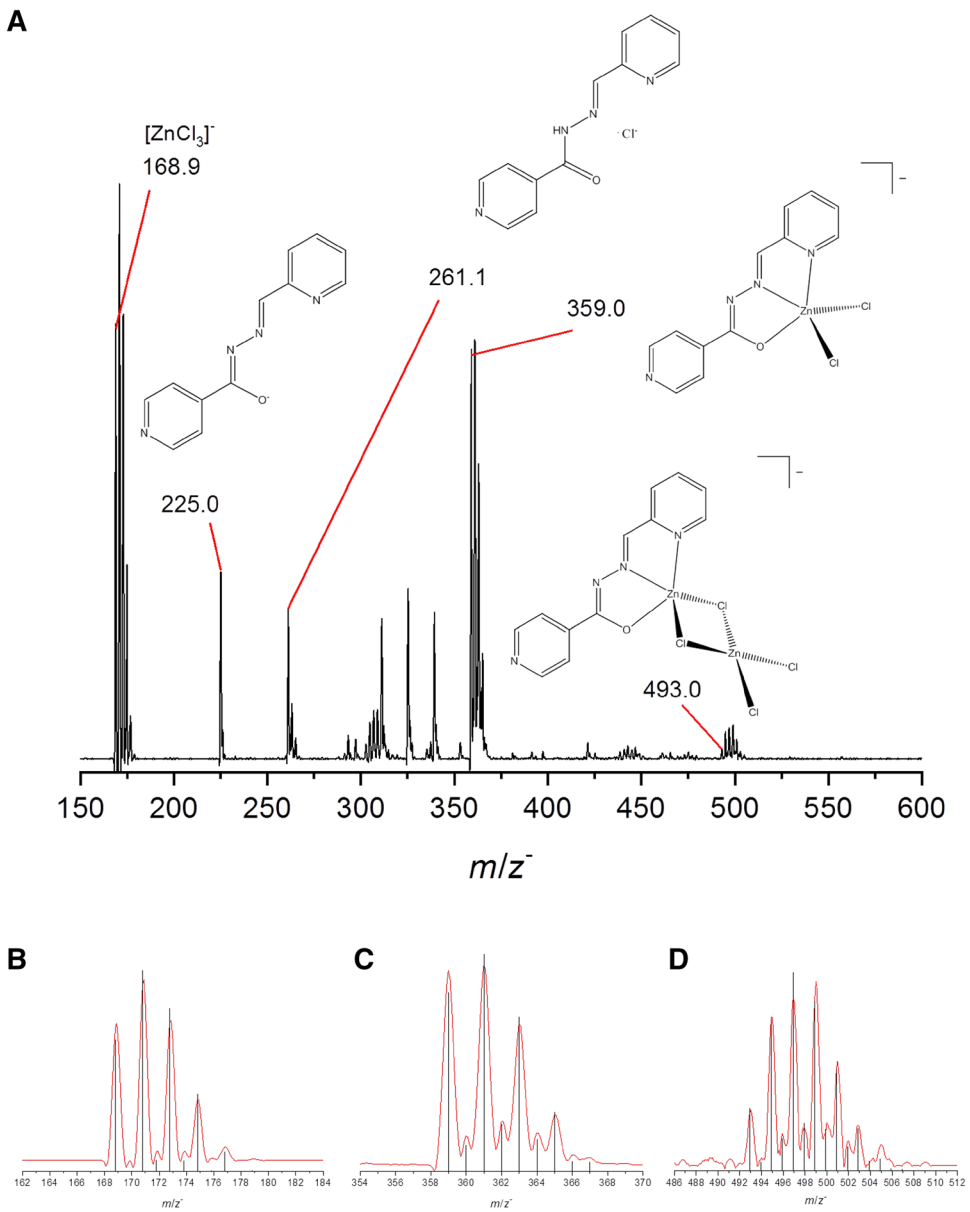

Fig. 7 **a** ESI-MS spectrum (negative mode) of (**1**) in a DMSO/methanol (5:95) mixture. **b** Isotope distribution of $[ZnCl_3]^-$. **c** Isotope distribution of $[ZnCl_2(PCIH)]^-$ ($C_{12}H_9N_4O\ Cl_2Zn^-$). **d** Isotope distribution of $[Zn_2Cl_4(PCIH)]^-$ ($C_{12}H_9N_4OCl_4Zn_2^-$). Experimental and calculated data are shown, respectively, as red and vertical black lines, respectively

known that the buffer conditions, peptide aggregation state and the methods used to calculate the constants are critical to the values obtained [48]. However, there is currently a consensus that K_d values for Zn^{2+} binding to Aβ(1–40) are of the order of 1–20 μM [12]. An ITC experiment demonstrated that the dissociation constant for the stoichiometric coordination of Zn^{2+} to Aβ(1–40) is 7 μM [49].

It is interesting to note that the binding constant that HPCIH exhibits in relation to zinc [$(1.43 \pm 0.05) \times 10^5$, reported in Table 5, calculated from ITC experiments as well] is of the same order of magnitude as that of the zinc(II) complex with the peptide, which is expected from a good MPAC. Since HPCIH's constant value presented herein is related to the formation of the ML_2 complex, it is natural that an excess of the compound is required to restore the free peptide's behavior.

Hydrophilic–lipophilic balance (log *P*)

The lipophilicity of a molecule is an important factor to study when considering a drug that needs to cross imperative membranes such as the blood–brain barrier to reach the brain and in this organ. This parameter was the first descriptor to be noted as important for CNS penetration. The hydrophilic–lipophilic balance is commonly quantified through the molecule's partition coefficient, log *P*. Optimal values of log *P* are considered between 0 and 3 [50]. HPCIH's experimental log *P* is 0.91 ± 0.12 (recovery

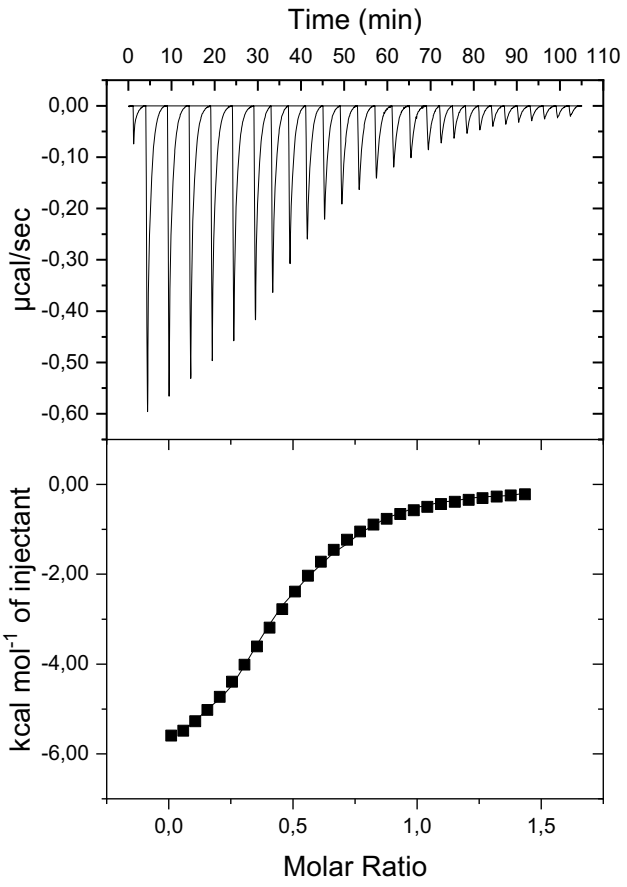

Fig. 8 Resulting titration curve of HPCIH with Zn^{2+} ions at 25 °C

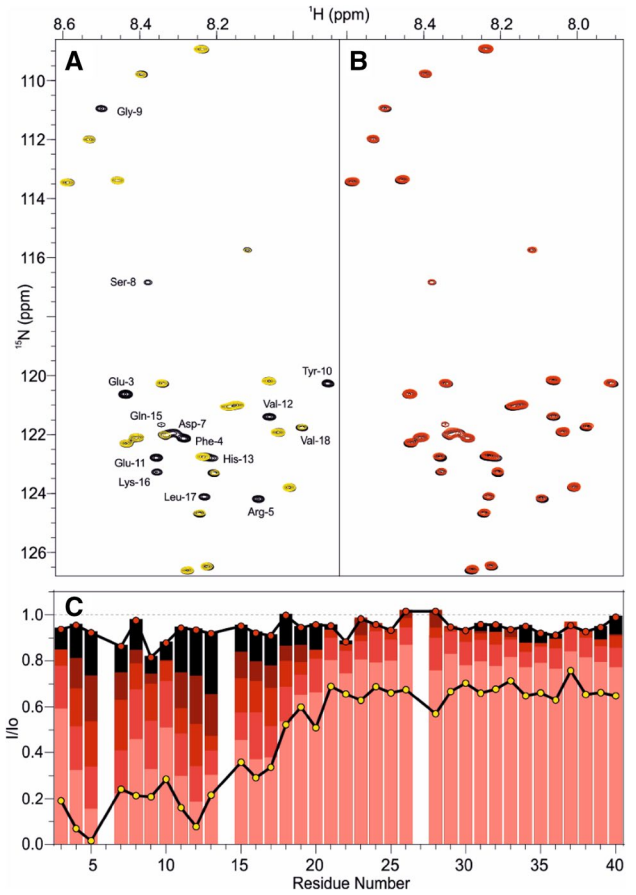

Fig. 9 Effect of HPCIH on Aβ–Zn^{2+} complexes. **a** Overlaid contour plots of the ^{1}H–^{15}N HSQC spectra of Aβ (50 µM) in the absence (black) and presence of 1 eq. of Zn^{2+} (yellow). The most affected residues are labeled. **b** Overlaid contour plots of the ^{1}H–^{15}N HSQC spectra of Aβ (50 mM) (black) and that recorded in the presence of 1 eq. of Zn^{2+}, followed by the addition of 10 eq. of HPCIH (red). **c** I/I_0 intensity profiles for the Aβ resonances in the presence of 1 equivalent of Zn^{2+} ions (yellow circles) before and after the addition of 1, 3, 5 and 10 equivalents of HPCIH (from light red to dark bars). Red circles highlight the almost complete recovery of signals after treatment with ten equivalents of HPCIH

Table 5 Stoichiometry, binding constant, enthalpy and entropy values of the reaction between HPCIH and Zn^{2+} at 25 °C

n	0.462 (*M*/*L* ratio)
K (L mol^{-1})	$1.43 \pm 0.05 \times 10^5$
ΔH (cal mol^{-1})	-6671 ± 77
ΔS (cal mol^{-1} deg^{-1})	1.22

of 98.2%), under the physiological compatible conditions of pH 7.4 and 37 °C. This value is in accordance to the calculated parameter (1.25) but differs substantially of that previously reported (1.98) [47].

Conclusions

The well-known ligand HPCIH was employed as a simplified chemical model for the promising hybrid metal-protein attenuating compound INHHQ in the study of interactions with Zn^{2+} ions, since both of them share the same aroylhydrazone moiety.

HPCIH showed to be stable in DMSO and methanol solutions, but undergoes slow hydrolysis in a 10% DMSO/water medium at room temperature. The determined log *P* (0.91 ± 0.1) of this ligand is in accordance to the theoretical value (1.25) and adequate to that expected for a compound that needs to cross the blood–brain barrier. NMR data suggest that a DMSO-d_6 solution of HPCIH contains three different forms of the ligand, being the (*E*)-keto-amine species the most abundant (85%).

Concerning the binding to zinc(II), both mononuclear (discrete) and polymeric complexes were observed in the solid state. In this context, the crystal structure of the novel

1D coordination polymer $\{[Zn_2Cl_2(HPCIH)_2]Cl_2\}_n$ was described. In a DMSO-d_6 solution of the ML complex $[ZnCl_2(HPCIH)]$ (**1**), both (*E*)-protonated (keto-amine) and (*E*)-deprotonated (enamine)-containing species are present. In addition to these entities, ESI-MS studies performed in a methanol/DMSO mixture allowed for the identification of the ML_2 stoichiometry species. In all the cases, HPCIH acts as a tridentate ligand through the pyridine and azomethine nitrogen atoms, and the carbonyl oxygen. ITC-based calculations were carried out to determine the formation constant of the ML_2 species, $\log \beta = 14.33$, which is in accordance to the literature. As far as we know, this is the first time in which the interactions of HPCIH with a single metal ion are studied, both in solution as in the solid state, in such a level of detail.

Like INHHQ, HPCIH is able to efficiently compete with Aβ(1–40) for Zn^{2+} ions in vitro, performing as expected for an MPAC, mainly because of its affinity for zinc, which is in the same order of magnitude of that of the Aβ peptide. The similarity between the behaviors of both ligands is remarkable. Therefore, we can conclude that the presence of the archetypical 8-hydroxyquinoline scaffold in INHHQ is not mandatory for its activity as an MPAC.

Taken together, the data presented herein point to aroylhydrazones, such as the compounds HPCIH and the previously published INHHQ, as encouraging MPACs for the treatment of AD, opening new paths for the bioinorganic research in the area.

Acknowledgements Nicolás A. Rey wishes to thank FAPERJ (Fundação Carlos Chagas Filho de Amparo à Pesquisa do Estado do Rio de Janeiro, Brazil) and CNPq (Conselho Nacional de Desenvolvimento Científico e Tecnológico, Brazil) for the research fellowships awarded. Daphne S. Cukierman thanks CNPq and CAPES (Coordenação de Aperfeiçoamento de Pessoal de Nível Superior, Brazil) for the scholarships granted. The authors are indebted to the Central Analytical Facility of the Department of Chemistry (PUC-Rio). The polycrystal X-ray diffraction analyses were done with the help of Prof. Dr. Roberto Avillez, at the X-Ray Diffraction Laboratory of the Chemical and Materials Engineering Department of PUC-Rio. The authors also thank LAMEM-UFF (Laboratório Multiusuário de Espectrometria de Massas da Universidade Federal Fluminense) for the mass spectrometry analyses.

References

1. Hardy JA, Higgins GA (1992) Alzheimer's disease: the amyloid cascade hypothesis. Science 256(5054):184–185
2. Kayed R et al (2004) Permeabilization of lipid bilayers is a common conformation-dependent activity of soluble amyloid oligomers in protein misfolding diseases. J Biol Chem 279(45):46363–46366
3. Klein WL, Krafft GA, Finch CE (2001) Targeting small Abeta oligomers: the solution to an Alzheimer's disease conundrum? Trends Neurosci 24(4):219–224
4. Lambert MP et al (1998) Diffusible, nonfibrillar ligands derived from Abeta1-42 are potent central nervous system neurotoxins. Proc Natl Acad Sci USA 95(11):6448–6453
5. Hane F, Leonenko Z (2014) Effect of metals on kinetic pathways of amyloid-β aggregation. Biomolecules 4(1):101–116
6. Hane F et al (2013) Cu(2+) affects amyloid-β (1–42) aggregation by increasing peptide-peptide binding forces. PLoS One 8(3):e59005
7. Deibel MA, Ehmann WD, Markesbery WR (1996) Copper, iron, and zinc imbalances in severely degenerated brain regions in Alzheimer's disease: possible relation to oxidative stress. J Neurol Sci 143(1–2):137–142
8. Azimi S, Rauk A (2011) On the involvement of copper binding to the N terminus of the amyloid Beta Peptide of Alzheimer's disease: a computational study on model systems. Int J Alzheimers Dis 2011:539762
9. Tõugu V, Karafin A, Palumaa P (2008) Binding of zinc(II) and copper(II) to the full-length Alzheimer's amyloid-beta peptide. J Neurochem 104(5):1249–1259
10. Huang X et al (2004) Trace metal contamination initiates the apparent auto-aggregation, amyloidosis, and oligomerization of Alzheimer's Abeta peptides. J Biol Inorg Chem 9(8):954–960
11. Craddock TJ et al (2012) The zinc dyshomeostasis hypothesis of Alzheimer's disease. PLoS One 7(3):e33552
12. Faller P, Hureau C (2009) Bioinorganic chemistry of copper and zinc ions coordinated to amyloid-beta peptide. Dalton Trans 7:1080–1094
13. Miura T et al (2000) Metal binding modes of Alzheimer's amyloid beta-peptide in insoluble aggregates and soluble complexes. Biochemistry 39(23):7024–7031
14. Yang DS et al (2000) Examining the zinc binding site of the amyloid-beta peptide. Eur J Biochem 267(22):6692–6698
15. Faller P, Hureau C (2012) A bioinorganic view of Alzheimer's disease: when misplaced metal ions (re)direct the electrons to the wrong target. Chemistry 18(50):15910–15920
16. Ventriglia M et al (2015) Zinc in Alzheimer's disease: a meta-analysis of serum, plasma, and cerebrospinal fluid studies. J Alzheimers Dis 46(1):75–87
17. Bucossi S et al (2011) Copper in Alzheimer's disease: a meta-analysis of serum, plasma, and cerebrospinal fluid studies. J Alzheimers Dis 24(1):175–185
18. Scott LE, Orvig C (2009) Medicinal inorganic chemistry approaches to passivation and removal of aberrant metal ions in disease. Chem Rev 109(10):4885–4910
19. Gaeta A et al (2011) Synthesis, physical-chemical characterisation and biological evaluation of novel 2-amido-3-hydroxypyridin-4(1H)-ones: iron chelators with the potential for treating Alzheimer's disease. Bioorg Med Chem 19(3):1285–1297
20. Budimir A (2011) Metal ions, Alzheimer's disease and chelation therapy. Acta Pharm 61(1):1–14
21. Cherny RA et al (2001) Treatment with a copper-zinc chelator markedly and rapidly inhibits beta-amyloid accumulation in Alzheimer's disease transgenic mice. Neuron 30(3):665–676
22. Drew SC (2017) The case for abandoning therapeutic chelation of copper ions in Alzheimer's disease. Front Neurosci 11:317
23. Squitti R et al (2017) Commentary: the case for abandoning therapeutic chelation of copper ions in Alzheimer's disease. Front Neurol 8:503
24. de Freitas LV et al (2013) Structural and vibrational study of 8-hydroxyquinoline-2-carboxaldehyde isonicotinoyl hydrazone—a potential metal-protein attenuating compound (MPAC) for the treatment of Alzheimer's disease. Spectrochim Acta A Mol Biomol Spectrosc 116:41–48
25. Hauser-Davis RA et al (2015) Disruption of zinc and copper interactions with Aβ(1–40) by a non-toxic, isoniazid-derived,

hydrazone: a novel biometal homeostasis restoring agent in Alzheimer's disease therapy? Metallomics 7:743–747
26. Cukierman DS et al (2017) A moderate metal-binding hydrazone meets the criteria for a bioinorganic approach towards Parkinson's disease: therapeutic potential, blood-brain barrier crossing evaluation and preliminary toxicological studies. J Inorg Biochem 170:160–168
27. Becker E, Richardson DR (1999) Development of novel aroylhydrazone ligands for iron chelation therapy: 2-pyridylcarboxaldehyde isonicotinoyl hydrazone analogs. J Lab Clin Med 134(5):510–521
28. Armstrong Claire M et al (2003) Structural variations and formation constants of first-row transition metal complexes of biologically active aroylhydrazones. Eur J Inorg Chem 2003(6):1145–1156
29. Mondal S, Naskar S, Deya AK, Sinn E, Eribalb C, Herronc SR, Chattopadhyaya SK (2013) Mononuclear and binuclear Cu(II) complexes of some tridentate aroyl hydrazones. X-ray crystal structures of a mononuclear and a binuclear complex. Inorg Chim Acta 398:98–105
30. Khandar AA, Afkhami FA, Hosseini-Yazdi SA, White JM, Kassel S, Dougherty WG, Lipkowski J, Van Derveer D, Giester G, Costantino F (2015) Anion influence in the structural diversity of cadmium coordination polymers constructed from a pyridine based Schiff base ligand. Inorg Chim Acta 427:87–96
31. Li L, Zhang YZ, Liu E, Yang C, Golen JA, Rheingold AL, Zhang G (2016) Synthesis and structural characterization of zinc(II) and cobalt(II) complexes based on multidentate hydrazone ligands. J Mol Struct 1110:180–184
32. Regland B et al (2001) Treatment of Alzheimer's disease with clioquinol. Dement Geriatr Cogn Disord 12(6):408–414
33. Adlard PA et al (2008) Rapid restoration of cognition in Alzheimer's transgenic mice with 8-hydroxy quinoline analogs is associated with decreased interstitial Abeta. Neuron 59(1):43–55
34. Zheng H et al (2005) Novel multifunctional neuroprotective iron chelator-monoamine oxidase inhibitor drugs for neurodegenerative diseases: in vitro studies on antioxidant activity, prevention of lipid peroxide formation and monoamine oxidase inhibition. J Neurochem 95(1):68–78
35. Gomes LM et al (2014) 8-Hydroxyquinoline Schiff-base compounds as antioxidants and modulators of copper-mediated Aβ peptide aggregation. J Inorg Biochem 139:106–116
36. Richardson D, Bernhardt PV, Becker EM (2006) Iron chelators and uses thereof. US6989397 B1
37. Bruker (2004) APEX2 user manual. Version 1.22 ed
38. Bruker (1999) SAINT Integration Software. Bruker AXS Inc., Madison
39. Sheldrick GM (2015) Crystal structure refinement with SHELXL. Acta Crystallogr C Struct Chem 71(Pt 1):3–8
40. Sheldrick GM (2008) A short history of SHELX. Acta Crystallogr A 64(Pt 1):112–122
41. International Tables for Crystallography C (2006)
42. Dolomanov et al (2009) OLEX2: a complete structure solution, refinement and analysis program. J Appl Crystallogr 42(2):339–341
43. Nakacjawa I, Shimanouchi T (1964) Infrared absorption spectra of aquo complexes and the nature of co-ordination bands. Spectrochim Acta 20:429–439
44. Bryson D, Nuttall RH (1970) The far infrared spectra of five coordinate complexes. Spectrochim Acta Part A 26:2275–2280
45. Frank CW, Rogers LB (1966) Infrared Spectral study of metal-pyridine, -substituted pyridine, and -quinoline complexes in the 667–150 cm^{-1} Region. Inorg Chem 5:615–622
46. Díaz-Torres R, Coordinating AS (2011) Ability of anions and solvents towards transition metals and lanthanides. Dalton Trans 40:10742–10750
47. Bernhardt PV et al (2007) Hydrazone chelators for the treatment of iron overload disorders: iron coordination chemistry and biological activity. Dalton Trans 30:3232–3244
48. Bush AI, Tanzi RE (2008) Therapeutics for Alzheimer's disease based on the metal hypothesis. Neurotherapeutics 5(3):421–432
49. Talmard C, Bouzan A, Faller P (2007) Zinc binding to amyloid-beta: isothermal titration calorimetry and Zn competition experiments with Zn sensors. Biochemistry 46(47):13658–13666
50. Pajouhesh H, Lenz GR (2005) Medicinal chemical properties of successful central nervous system drugs. NeuroRx 2(4):541–553